JOURNAL OF GEOPHYSICAL RESEARCH, VOL. 107, NO. D2, 4013, 10.1029/2001JD000410, 2002

Simulation of a biomass-burning plume: Comparison of model results with observations

J. Trentmann,[1] M. O. Andreae,[1] H.-F. Graf,[2] P. V. Hobbs,[3] R. D. Ottmar,[4] and T. Trautmann[5,6]

Received 31 January 2001; revised 27 June 2001; accepted 27 June 2001; published 25 January 2002.

[1] We have simulated the dynamical evolution of the plume from a prescribed biomass fire, using the active tracer high-resolution atmospheric model (ATHAM). Initialization parameters were set to reflect the conditions during the fire. The model results are compared with airborne remote-sensing and in situ measurements of the plume. ATHAM reproduces the injection height (250–600 m) and the horizontal extent of the plume (~4 km) with good accuracy. The aerosol mass concentrations are underestimated but still in the range of the observations. Remaining differences between the model results and the measurements are attributed to limited meteorological and fire emission information. Additionally, radiative transfer simulations using in situ measurements of the aerosol properties are performed. A comparison of the measured and simulated reflected solar flux shows an underestimation by the model over the ocean surface, which is most likely due to an underestimation of the aerosol optical depth in the model. The instantaneous radiative forcing was calculated to -36 W m^{-2} over land and -58 W m^{-2} over the ocean for a solar zenith angle of 47° and an optical depth of unity, consistent with previous studies. Overall, it appears that ATHAM is a valuable tool for the examination of transport processes within biomass-burning plumes and, together with a chemical and microphysical module, is suitable for studies of the interaction between transport, chemistry, and microphysics within such plumes. *INDEX TERMS:* 0305 Atmospheric Composition and Structure: Aerosols and particles (0345, 4801), 0368 Atmospheric composition and structure: Troposphere-constituent transport and chemistry, 3329 Meteorology and Atmospheric Dynamics: Mesoscale meteorology, 3359 Meteorology and Atmospheric Dynamics: Radiative processes; *KEYWORDS:* Biomass burning, SCAR-C, aerosol transport, aerosol optical properties

1. Introduction

[2] Vegetation fires are known to be a major contributor to the global budgets of several trace gases (e.g., CO, CH_4, and NO_x) as well as aerosol particles [*Crutzen and Andreae*, 1990]. The regional and global effects from fire emissions have been demonstrated in field campaigns, such as the Transport and Atmospheric Chemistry near the Equator-Atlantic (TRACE-A), Southern African Fire-Atmosphere Research Initiative (SAFARI) [*Andreae et al.*, 1996], and the Smoke, Clouds, and Radiation-Brazil (SCAR-B) [*Kaufman et al.*, 1998], and in modeling studies [e.g., *Chatfield et al.*, 1998; *Galanter et al.*, 2000]. The regional and global impacts of vegetation fires on atmospheric composition depend on the processes that take place near the fire, for example, the height of the injection of the emissions [*Liousse et al.*, 1996], the nonlinear production of ozone [*Poppe et al.*, 1998], and the possible formation of clouds and scavenging of the emissions [*Radke et al.*, 1991]. Therefore *Crutzen and Carmichael* [1993] concluded that small-scale models "complemented with atmospheric chemistry and emission description could provide important insights into the chemistry and scavenging of trace gases and aerosols in the near-source region and would be of great assistance in the development of parameterizations needed by regional and global models."

[3] However, until now, no such model has existed. Existing models of coupled fire dynamics and meteorology focus mainly on the fire dynamics [*Clark et al.*, 1996; *Grishin*, 1996] and do not include detailed atmospheric processes. The only numerical simulation of the atmospheric transport of particles from a vegetation fire and their interaction with clouds did not include quantitative comparisons with observations [*Penner et al.*, 1991].

[4] Here we present model simulations of the atmospheric transport of aerosol emissions from a vegetation fire using the nonhydrostatic active tracer high-resolution atmospheric model (ATHAM) [*Oberhuber et al.*, 1998; *Herzog et al.*, 1998]. The atmospheric conditions and the heat and particle fluxes from the fire used in our model simulation correspond to those of an actual prescribed fire conducted on September 21, 1994, during the Smoke, Cloud, and Radiation-C (SCAR-C) experiment in the Pacific Northwest of the United States [*Kaufman et al.*, 1996]. The simulated aerosol concentrations are compared with in situ and remote-sensing measurements of the smoke plume from this fire [*Kaufman et al.*, 1996; *Hobbs et al.*, 1996; *Martins et al.*, 1996].

[5] The primary aim of this paper is the evaluation of the general features of the model results, rather than a detailed comparison with the observations. A comprehensive comparison between model results and observations of natural biomass-burning plumes is probably impossible because of the high temporal and spatial variability of the emissions, which cannot be adequately represented in this kind of model. The model was

[1]Biogeochemistry Department, Max Planck Institute for Chemistry, Mainz, Germany.
[2]Max Planck Institute for Meteorology, Hamburg, Germany.
[3]Department of Atmospheric Sciences, University of Washington, Seattle, Washington, USA.
[4]Seattle Forestry Science Laboratory, Seattle, Washington, USA.
[5]Institute of Atmospheric Physics, University of Mainz, Mainz, Germany.
[6]Now at Institute for Meteorology, University of Leipzig, Leipzig, Germany.x

0148-0227/02/2001JD000410

Figure 1. Photograph of the smoke plume produced from the Quinault prescribed fire at 1250 LT, at ~100 min after the ignition. (Photo taken by R. Ottmar, reproduced from *Kaufman et al.* [1996] with the permission of the MIT Press.)

initialized on the basis of observational data in order to constrain model assumptions as far as possible. No sensitivity studies are presented here, because the aim of the paper was to describe and evaluate our model. Further studies on different biomass-burning plumes, including sensitivity tests using ATHAM, are under way.

2. Model Description

[6] ATHAM was used for the study of eruptive volcanic plumes by *Graf et al.* [1999]. Only a short description of the model is given here. For a more detailed description of the model the reader is referred to *Oberhuber et al.* [1998] and *Herzog et al.* [1998].

[7] The nonhydrostatic plume model ATHAM has a modular structure, which allows easy coupling of new modules. Existing modules treat the dynamics, turbulence, transport, cloud microphysics, gas scavenging, and radiation. The Navier-Stokes equations for the volume-mean of a gas-particle mixture, including the transport of active tracers, are solved in the dynamical part of the model. Active tracers influence the simulated density and heat capacity within the model grid boxes and therefore affect the modeled dynamics. Turbulent exchange coefficients for each dynamic variable are computed with a turbulence closure scheme. Atmospheric transport of the active and passive tracers is treated using the method of *Smolarkiewicz* [1984], and the advection of heat and turbulent quantities are described using a scheme similar to *Crowley* [1968]. The cloud microphysics is based on a Kessler-type parameterization and describes condensation and formation of precipitation as well as the scavenging of soluble gases [*Textor*, 1999]. The fire is represented by heat and particulate fluxes into the lowest vertical model layer at prescribed grid boxes. There is no feedback from the atmospheric wind field on the fluxes from the fire.

[8] The calculation of the heating rates and the radiative forcing are performed with the radiative transfer model described by *Loughlin et al.* [1997], which is based on the two-stream practical improved flux method (PIFM) [*Zdunkowski et al.*, 1982] and includes radiative effects of gases, aerosols, and clouds. Alternatively, the radiative transfer model described by *Langmann et al.* [1998] can be used. In the present study the PIFM model is used. According to *Briegleb et al.* [1986], we set the surface albedo for land to 4% for $\lambda < 690$ nm and 25% for $\lambda > 690$ nm. For the ocean surface an albedo of 6% for the diffuse light is used, while for the direct light the solar zenith angle dependency is taken into account [*Briegleb et al.*, 1986].

[9] ATHAM is formulated three-dimensionally on a horizontally and vertically stretched Cartesian grid with an implicit time stepping scheme. Besides the three-dimensional (3-D) model version a 2-D Cartesian and a 2-D cylindrical version exist. In this study only 3-D model results are presented.

3. SCAR-C Experiment

[10] The SCAR-C experiment was conducted in September 1994 in the Pacific Northwest of the United States. A detailed description of the campaign is given by *Kaufman et al.* [1996] and *Hobbs et al.* [1996]. Only an overview is given here.

[11] The emphasis of SCAR-C was "on measuring the entire process of biomass burning, including ground-based estimates of fuel consumption, airborne sampling of the smoke aerosols and trace gases, and airborne and spaceborne remote sensing of both the fires and the smoke" [*Kaufman et al.*, 1996]. In the present study we focus on a prescribed fire on September 21, 1994, on the Pacific Coast of Washington State in the Quinault Indian Reservation on the Olympic Peninsula (47.32°N, 124.27°W). The Quinault fire was a 19.4-ha clearcut burn, with fuel consisting of the dry remnants of large western red cedar debris left over from logging [*Kaufman et al.*, 1996]. Measurements before and during this fire included fuel loadings, airborne in situ measurements of trace gases and particles, and airborne remote-sensing observations of the fire and the smoke plume from the University of Washington's Convair C-131A and NASA's ER-2 research aircraft [*Kaufman et al.*, 1996; *Hobbs et al.*, 1996; *Martins et al.*, 1996]. The ignition sequence was started at 1105 local time (LT).

[12] Figure 1 shows a photograph of the smoke plume above the fire at ~100 min after the ignition. The smoke was first lofted directly above the fire up to ~600 m. It was then transported by the prevailing wind out over the Pacific Ocean (Figure 2).

[13] Figure 2 was obtained from spectral measurements of the Airborne Visible and Infrared Imaging Spectrometer (AVIRIS) [*Green et al.*, 1998] on board the NASA ER-2 aircraft. The high variability in the smoke loading is easily seen in Figures 1 and 2.

[14] Because the plume remained intact and was readily discernible over a long distance and there are no terrain-induced effects over the ocean, this fire presents an excellent opportunity to study the processes within a biomass-burning plume using an atmospheric model. Besides the detailed analysis of the in situ measurements [*Hobbs et al.*, 1996; *Martins et al.*, 1996], the remote-sensing observations of the smoke plume have been used in previous studies for the retrieval of aerosol properties [*Tanré et al.*, 1997] and for a comparison of remote-sensing retrieved

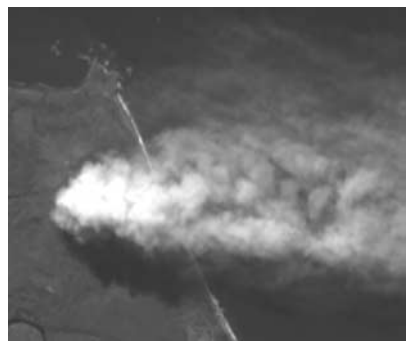

Figure 2. View of the smoke plume from the Quinault prescribed fire derived from spectral measurements taken from the AVIRIS instrument on board the ER-2 aircraft at 1243 LT, ~95 min after ignition. Calibrated Airborne Visible and Infrared Imaging Spectrometer (AVIRIS) data were obtained from Robert Green, Jet Propulsion Laboratory (JPL).

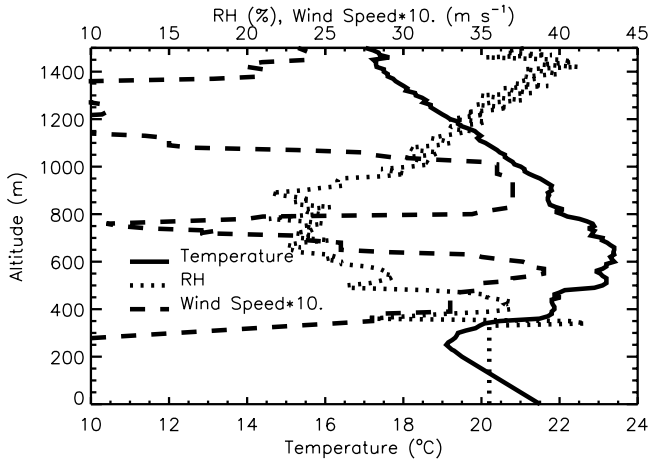

Figure 3. Initial atmospheric profiles of the temperature (lower axis), relative humidity (RH) (upper axis), and wind speed (upper axis) up to an altitude of 1.5 km used in the model simulations. Above 320 m, aircraft measurements are used. For the values below this altitude, see the text.

aerosol properties with the in situ measurements [*Gassó and Hegg*, 1998].

4. Model Initialization

[15] In the following we present model simulations of the Quinault fire using ATHAM. In this section the model setup for the simulations, the atmospheric initial conditions, the emissions of the fire, and the calculated optical aerosol properties are presented. Initialized with the meteorological variables, ATHAM calculates the wind field resulting from the thermal forcing of the fire. In particular, the induced vertical wind due to the heating from the fire is simulated. The emitted aerosols are transported with this simulated wind.

4.1. Model Setup

[16] The model domain (x, y, z) of the 3-D ATHAM version was set to 35 km × 28 km × 3.75 km, with a minimal grid spacing of 50 m × 50 m × 20 m in the central part of the model domain, where the fire forcing was initialized. The number of grid boxes in the x, y, and z direction was 120, 110, and 80, respectively, resulting in 1,056,000 model grid boxes. The time step is determined automatically by the Courant-Friedrichs-Lewy (CFL) criterion; it lies usually in the range 3–8 s. The model simulations were started at 1100 LT, with a spin-up time of 6 min before the ignition of the fire. In this paper we present model results at 100 min after fire ignition.

4.2. Initial Profiles of Meteorological Variables

[17] The atmospheric initial conditions for the simulations are taken from airborne measurements aboard the Convair C-131A before the ignition of the fire (between 1100 LT and 1111 LT); these initial profiles are shown in Figure 3.

[18] The airborne measurements were available between 320- and 1890-m altitude. Above 1890 m, atmospheric conditions from a radiosonde (CODIAC, Joint Office for Science Support (JOSS) data system, 1999)(available at http://www.joss.ucar.edu/codiac/), supplemented by data from the U.S. Standard Atmosphere [*Anderson et al.*, 1986], were used. From the surface up to 200 m a dry adiabatic lapse rate was assumed. From 200 to 320 m an increase in temperature to the values measured at 320 m was taken on the basis of other temperature profiles measured during the flight of the Convair 131A. Since the relative humidity does not affect the dynamic evolution of the model simulations, it was set to a constant value below 300 m. The wind speed was assumed to decrease to zero below 225 m because of the visual observations shown in Figure 1. The atmospheric conditions above 1500 m do not influence the model results and are not included in Figure 3. Also not shown in Figure 3 is the wind direction, which is, however, included in the model simulations: between 300 and 800 m, easterly winds prevailed, and between 800 and 1100 m the wind changed to northerly.

[19] The main feature of the atmospheric profile is the strong temperature inversion between 300 and 600 m. The temperature profile above 600 m is dry stable with a lapse rate of −0.73 K/100 m. The relative humidity is generally quite low with maximum values around 40%. The maximum wind speed is 4 m s^{-1}.

[20] The whole model domain was initialized with the same atmospheric profile. Since the region of interest was located near the coast, the assumption of horizontal homogeneity of the atmosphere is probably not fulfilled in reality and may lead to discrepancies between the model results and observations. Unfortunately, there is no information about the horizontal variations of the atmospheric profile before the fire.

4.3. Fire Emissions

[21] Fire emissions of energy and particles (shown in Figure 4) were obtained using the emission production model (EPM) [*Sandberg and Peterson*, 1984; *Ferguson et al.*, 2000]. EPM takes into account the loading, consumption, and moisture of different fuel size classes and the duff. Additionally, information about the method of ignition and the overall size of the fire is taken into account. The parameters used for the Quinault fire are given in Table 66.1 of *Hobbs et al.* [1996]. With theses parameters, EPM calculates the time-dependent emissions of energy, particulate matter (diameter <2.5 μm, PM2.5), and some trace gases (CO_2, CO, CH_4), accounting for different phases of the fire (flaming and smoldering). The emission factors are taken from the Compilation of Air Pollutant Emission Factors (AP-42) provided by the United States Environmental Protection Agency (U.S. EPA) (available at http://www.epa.gov/ttn/chief/ap42/index.html). For the Quinault fire the values for the PM2.5 emission factor were between 6 and 17 g kg^{-1}, depending on the fuel type and the phase of the fire. The modeled values for the total energy emissions are multiplied by a factor 0.55 to account only for convective energy [*McCarter and Broido*, 1965; S. Ferguson, personal communication, 1999]. This factor depends on several characteristics of the fuel. The value used here is in the middle of the commonly accepted range of 0.4–0.8 [*Fergu-*

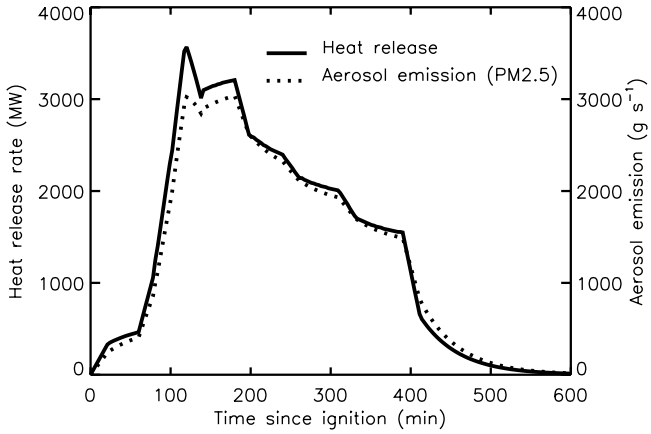

Figure 4. Convective heat and particle (<2.5-μm diameter) emission over time for the Quinault fire, calculated using the emission production model (EPM).

son et al., 2000]. These spatially integrated emissions are introduced into ATHAM as fluxes into the lowest model layer. The spatial distribution of fire pixels in the model was set following Figure 65.2 of *Kaufman et al.* [1996]. The 10 subunits were "ignited" in the model simulations according to the information from the ignition sequence of the U.S. Forest Service. The total ignition time was 35 min.

4.4. Aerosol Optical Properties

[22] To simulate atmospheric radiative transfer and calculate atmospheric heating rates, the wavelength-dependent aerosol optical properties are needed. If the number distribution and the refractive index of the aerosol particles are known, and if the particles are assumed to be spherical, their optical properties can be calculated from Mie theory. The number distribution of the aerosol in the smoke plume was measured from the aircraft using three instruments as described by *Hobbs et al.* [1996] and *Gassó and Hegg* [1998]. For the present study we used a size distribution that was measured with a differential mobility particle sizing system (DMPS) between 0.01- and 0.56-μm diameter at a distance of 7.6 km from the fire (see Figure 5).

[23] This size distribution is assumed to be representative of most parts of the plume. As shown by *Gassó and Hegg* [1998], the size distribution varied along the length of the plume, especially close to the fire. In the present study we focus on the plume properties farther downwind, where the particle size distribution did not change so much. Also included in Figure 5 is a fitted curve based on the sum of two log-normal distributions. The resulting effective particle radius of 0.14 μm is in reasonable agreement with the value of 0.127 μm given by *Gassó and Hegg* [1998]. The fitted curve is used for the calculation of the wavelength-dependent optical properties of the aerosol particles.

[24] The black carbon (BC) content of the aerosol particles determines their absorbing properties. For the particles from the Quinault fire the BC mass content was determined to be 8 ± 1.2% from reflectance technique and 7.7% from thermal measurements [*Martins et al.*, 1996]. A value of 8% was used for the simulations of the optical properties. The remaining particle mass

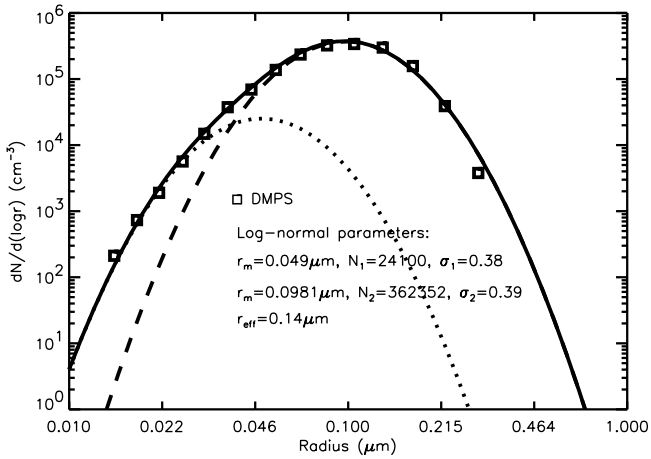

Figure 5. Differential mobility particle sizing system (DMPS) measurement of the particle number size distribution in the range 0.005- to 0.28-μm radius (squares) at an approximate distance of 7.6 km from the fire at 1247 LT (~100 min after ignition). Also included is the sum of two log-normal distributions (thick line) as well as the two log-normal distributions (thin dotted and thin dashed). The sum of the log-normal distributions is used in the calculation of the optical properties of the particles.

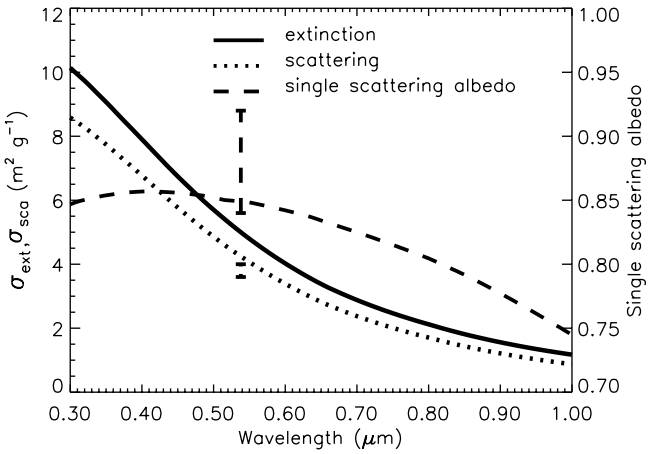

Figure 6. Mass extinction (left axis), mass scattering (left axis), and single-scattering albedo (right axis) calculated from the assumed size distribution and composition of the particles using Mie theory. The bars give the corresponding measurements taken from *Hobbs et al.* [1996] and *Reid* [1998].

is assumed to be organic carbon (OC) [*Martins et al.*, 1996; *McDow et al.*, 1996].

[25] A wavelength-dependent refractive index of the aerosol particles has to be assumed for the Mie calculations of the optical properties. For the BC part the values from *Fenn et al.* [1985] for soot are used. In the wavelength region between 2 and 19 μm, the values of *Sutherland and Khanna* [1991] are taken for OC. Outside this wavelength range, only very limited information about the refractive index of OC exists. The values commonly used are between 1.43 and 1.54 for the real part of the refractive index and 0 and 0.0035 for the imaginary part with little wavelength dependence [*Sloane*, 1983; *Holben et al.*, 1991; *Krekov*, 1992; *Ross et al.*, 1998]. As the refractive index of ammonium sulfate, $(NH_4)_2SO_4$, shows a similar behavior, we followed the work of *Grant et al.* [1999] and used the wavelength-dependent refractive index of ammonium sulfate from *Toon et al.* [1976] for OC in the remaining wavelength region. In the visible spectral range we use values between 1.52 and 1.54 for the real part of the refractive index and set the imaginary part to zero.

[26] The effect of humidity on the optical properties is neglected in this study, because the relative humidity was low (<40%). Additionally, the humidification factor for biomass-burning aerosol is small compared to those for industrial and urban aerosols [*Kotchenruther and Hobbs*, 1998].

[27] The refractive index of the internal mixture of BC and OC was calculated using the Maxwell-Garnett mixing rule [*Bohren and Huffman*, 1983], assuming the same density for BC and OC. The resulting value of the imaginary refractive index (n = 1.55–0.034i at 550 nm) is only slightly different from the value obtained from the volume mixing rule [*Horvath*, 1993].

[28] The optical properties of the particles were calculated using a Mie code [*Bohren and Huffman*, 1983] based on the particle size distribution and the calculated refractive index; they are shown in Figure 6 for the most relevant spectral range.

[29] For the density of the aerosol particles a value of 1.53 g cm^{-3} was calculated from the values given by *Martins et al.* [1996]. The calculated values of the mass scattering efficiency and the single-scattering albedo at 550 nm are 4.06 m^2 g^{-1} and 0.848, respectively. These numbers are in satisfactory agreement with the measured values of 3.8 ± 0.2 m^2 g^{-1} for the scattering efficiency and 0.84–0.92 for the single-scattering albedo [*Hobbs et al.*, 1996; *Reid*, 1998].

[30] Use of the aerosol optical properties in the radiative transfer model requires the determination of the values for the model wavelength bands. For this purpose the optical properties with high spectral resolution are weighted by the extraterrestrial solar flux [*Wehrli*, 1985] (available at ftp://ftp.pmodwrc.ch/publications/pmod615.asc) and averaged over the wavelength intervals of the radiative transfer model. The values used are listed in Table 1.

[31] Although the radiative transfer model includes the solar and the terrestrial spectrum, only the solar spectrum is taken into account in this study.

5. Model Results and Comparison With Measurements

[32] In this section the model results are compared with in situ and remote-sensing measurements of the smoke plume. Using the present model setup, the simulation time is limited to 100 min, during which the fire emissions reach the border of the model domain. Nearly all observations used for the com-

Table 1. Optical Properties of the Aerosol Particles Used in the Radiative Transfer Calculation[a]

Spectral Interval, nm	σ_{ext}, m^2 g^{-1}	σ_{sca}, m^2 g^{-1}	ω	g
200—690	5.80	4.93	0.85	0.64
690—1300	1.62	1.27	0.78	0.47
1300—1900	0.39	0.22	0.56	0.24
1900—2500	0.18	0.06	0.33	0.13
2500—3510	0.20	0.018	0.088	0.076
3510—4000	0.15	0.008	0.055	0.046

[a] Given are the mass extinction coefficient σ_{ext}, the mass scattering coefficient σ_{sca}, the single-scattering albedo ω, and the asymmetry parameter g. These values were obtained by energy-weighted averaging of the spectral high-resolved optical properties shown in Figure 6.

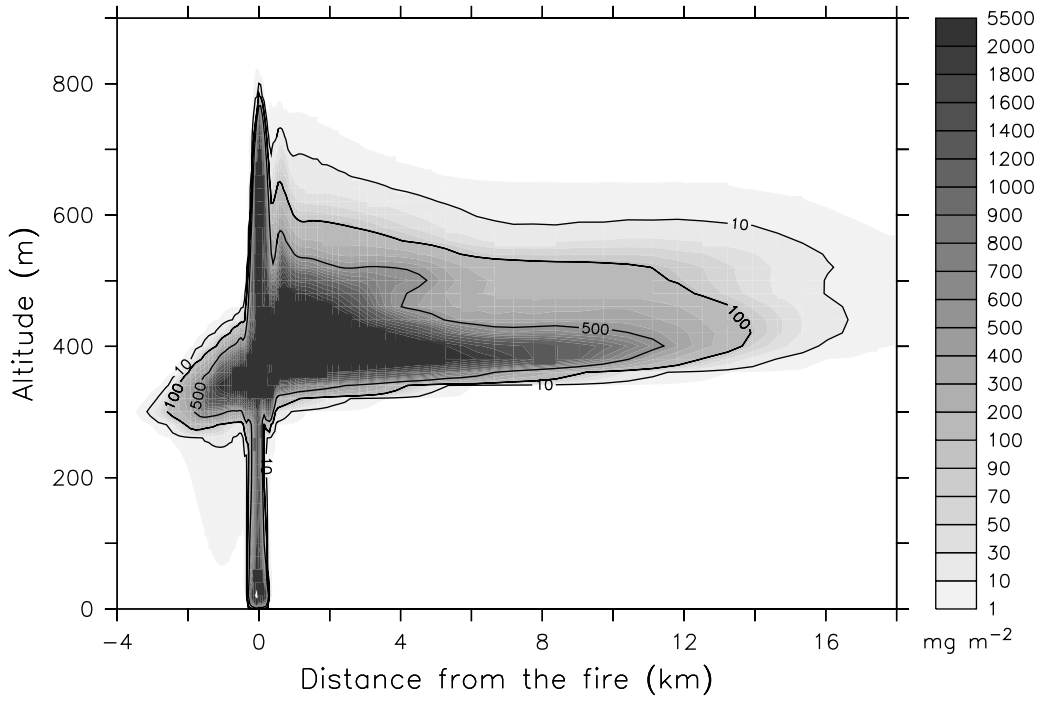

Figure 7. Simulated horizontally integrated aerosol mass concentrations after 100 min of simulation time. The unit of the contour lines is mg m^{-2}.

parison are from 1230 to 1300 LT, i.e., 85–115 min after ignition. Within this time the general appearance of the plume did not change significantly. Nevertheless, we used modeled aerosol concentrations temporally as close to the observations as possible.

[33] A principal limitation in the comparison is that small-scale fluctuations in the plume due to the fire forcing and small-scale atmospheric turbulence cannot be reproduced realistically by ATHAM. This is due to limited information on the temporal and spatial development of the fire emissions and the limited spatial resolution of the model. Nevertheless, the goal of this study was to show that the general feature of the plume can be reproduced reasonably well and that ATHAM is suitable for sensitivity studies of processes within biomass-burning plumes.

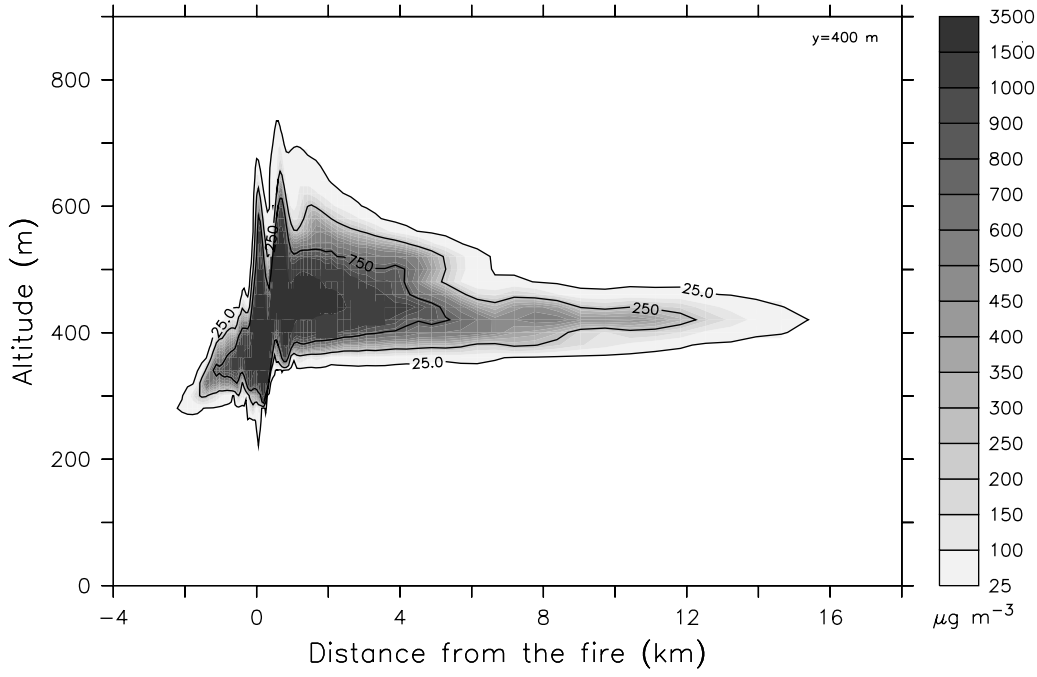

Figure 8. Simulated vertical cross section of the aerosol mass concentrations along the length of the plume 100 min after ignition at a distance of 400 m behind the center of the fire. The unit of the contour lines is μg m^{-3}.

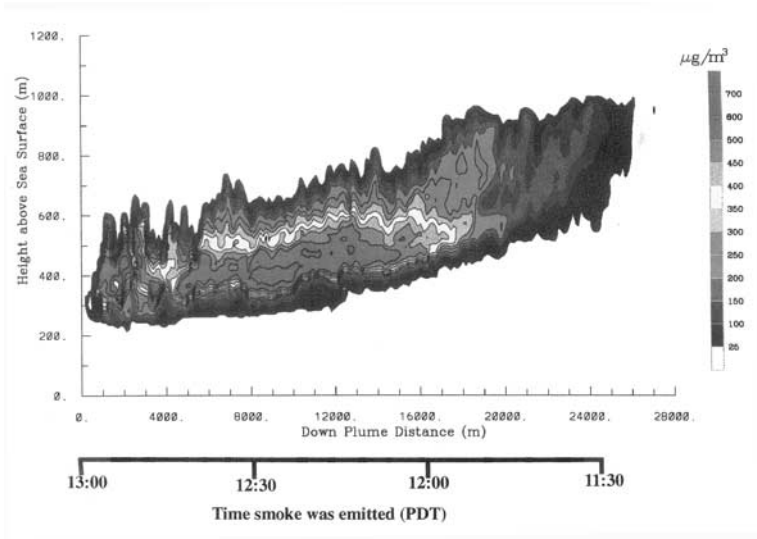

Figure 9. Vertical cross section of aerosol mass concentrations along the length of the smoke plume obtained with an airborne LIDAR between 1254 and 1259 LT (~110 min after ignition). Also included is the approximate time when the smoke was emitted (calculated from the wind speed). (Reproduced from *Hobbs et al.* [1996] with the permission of the MIT Press.)

[34] Shown in Figure 7 is the simulated horizontally integrated aerosol mass in the plume, which reveals the general features of the simulated plume. A quantitative comparison with observations is given in the following subsections.

5.1. Comparison of Simulations With Measurements

5.1.1. Remote-sensing observations. [35] The simulated aerosol mass concentration along the plume at a distance of 400 m behind the center of the fire is shown in Figure 8. This result is compared with airborne LIDAR measurements [*Hobbs et al.*, 1996] in Figure 9.

[36] These downward pointing measurements were taken at 1254–1259 LT (~110 min after the ignition) from the University of Washington's Convair C-131A aircraft (for a description of the aircraft and its instrumentation, see *Hobbs et al.* [1991]). The observed injection height of the aerosol particles was between 250 and 600 m, compared to 300–700 m in the model simulations. The latter height range is determined by the atmospheric profile (in this case by the strong temperature inversion between 300 and 600 m) and the heat emissions from the fire. Downwind of the fire the thickness of the aerosol plume derived from the LIDAR measurements is ~300 m, whereas in the model simulations the plume is only ~100 m thick. The simulated downwind aerosol concentra-

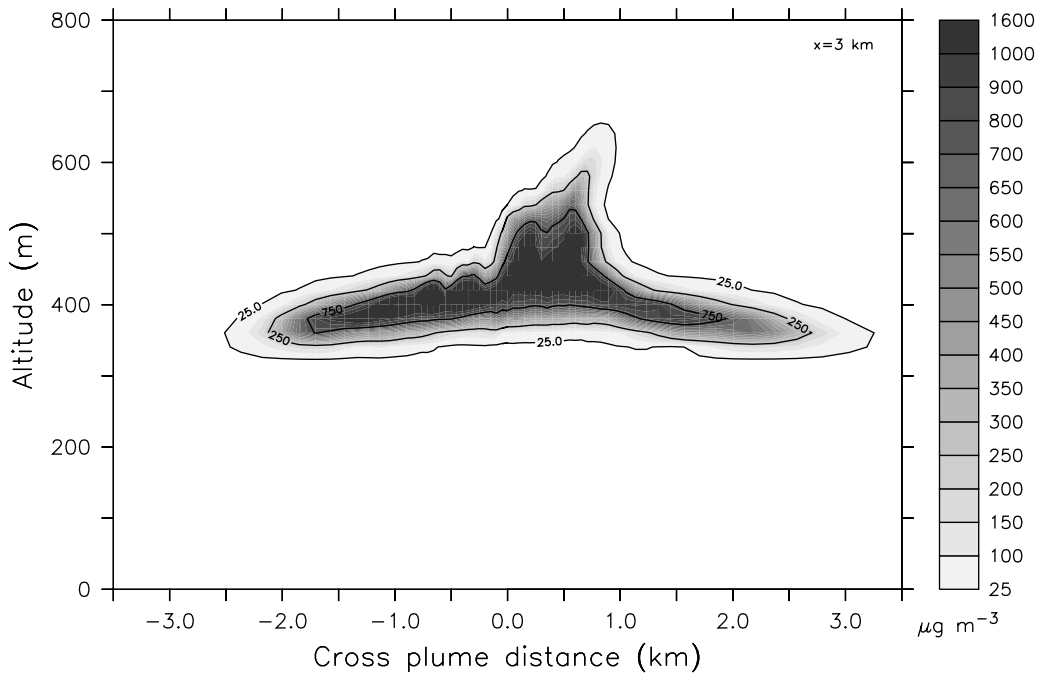

Figure 10. Simulated aerosol mass concentrations across the plume at a distance of 3 km from the fire 100 min after ignition. The unit of the contour lines is μg m^{-3}.

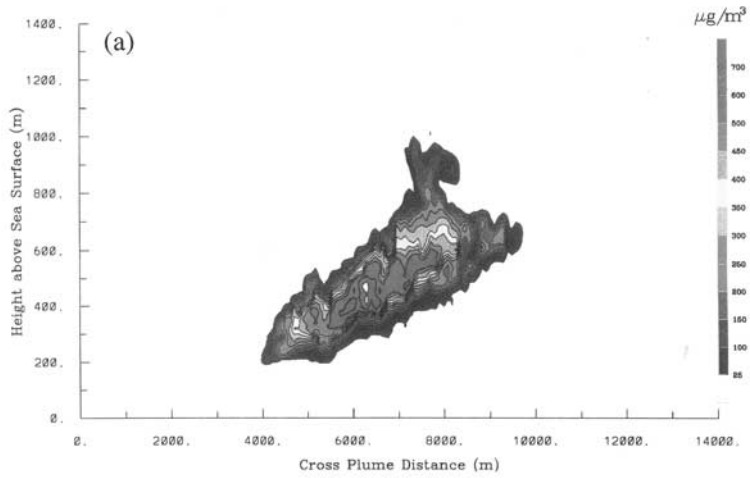

Figure 11. Vertical cross section across the width of the smoke plume obtained at 1339 LT (∼150 min after ignition) 3 km downwind of the fire. (Reproduced from *Hobbs et al.* [1996] with the permission of the MIT Press.)

tions are between 25 and 1000 μg m^{-3} and thus in the same range as the measured aerosol concentrations. The maximum distance from the fire of the smoke aerosols in the measurements is ∼28 km (after ∼110 min), whereas in the simulations the aerosols traveled a distance of only ∼16 km (after 100 min). The observed aerosol plume exhibited a strong lofting downwind, which is not as intense in the simulated plume.

[37] The simulated aerosol mass concentration across the plume at a distance of 3 km from the fire is shown in Figure 10. This can be compared with the LIDAR measurements obtained at 1339 LT (∼2.5 hours after ignition) 3 km downwind of the fire [*Hobbs et al.*, 1996] shown in Figure 11.

[38] The simulated aerosol plume is rather flat at the lower boundary, while the observations show a horizontal gradient of the lower plume boundary. The reasons for this discrepancy are most probably inhomogenities in the atmospheric conditions, which were not accounted for in the model. The mass concentrations within the plume in the simulations, as well as in the observations, are around 700 μg m^{-3}. The overall width of the plume in the simulations is ∼5.5 km, which is in close agreement with the observations (∼6 km). It is interesting that the peak at the 7500-m cross-plume distance in the observations also appears in the simulations (at 500 m cross-plume distance). In the model simulations, and possibly also in the observations, this peak is caused by intense vertical transport of the smoke directly above the fire where the heat-produced convection intruded into the stable atmospheric layer. Similar ''overshooting'' has been observed in simulations of large-scale fires [*Penner et al.*, 1986].

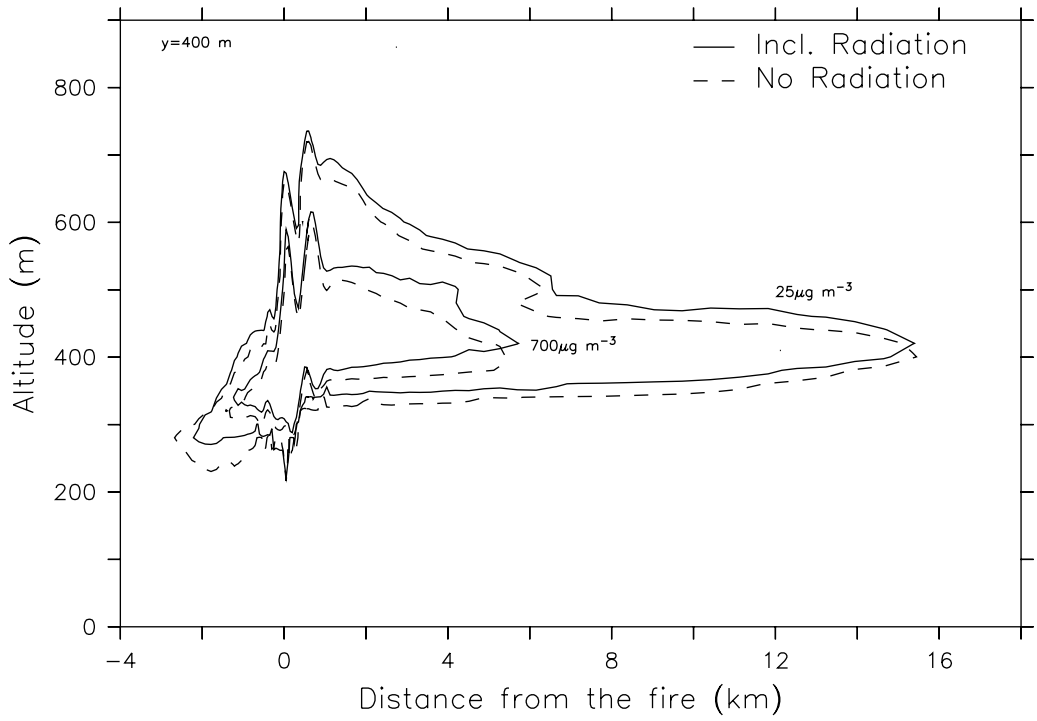

Figure 12. Simulated vertical aerosol mass concentrations along the length of the plume at a distance of 400 m behind the center of the fire 100 min after ignition, including and neglecting the solar heating of the aerosol particles.

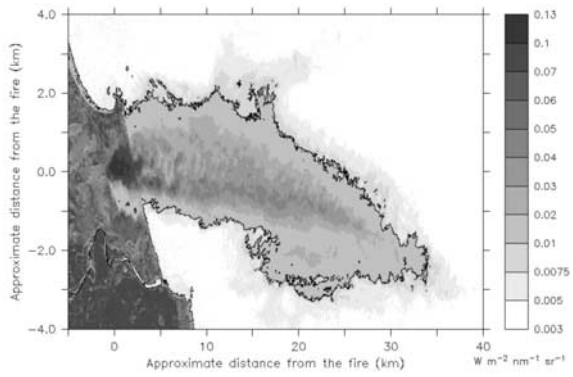

Figure 13. Reflected radiances at 850 nm, measured on board the ER-2 aircraft using the AVIRIS instrument between 1243 and 1248 LT (∼100 min after ignition). Calibrated AVIRIS data were obtained from Robert Green, JPL.

[39] In general, the agreement between the model results and the LIDAR measurements is satisfactory for the purpose of this study. The injection height and the overall particle concentrations are reproduced reasonably well. One major difference is found in the maximum travel distance. This is related to a higher wind speed over the ocean, which was not included in the model simulations. Another feature that is not reproduced well by the model is the downwind lofting of the aerosol plume. This lofting may be due to the heating of the aerosols by the absorption of solar radiation, as observed in fossil fuel burns [*Radke et al.*, 1990; *Herring and Hobbs*, 1994]. In order to test this hypothesis, we performed a model simulation without accounting for the interaction of the aerosol particles with solar radiation and therefore neglecting the solar heating of the aerosols.

[40] Figure 12 shows the impact of the solar heating on the simulated aerosol concentrations. The simulation including the aerosol heating shows a lofting of the plume downwind of the fire, although it is much smaller than in the observations. We conclude that the observed lofting was probably caused by changing atmospheric conditions over the ocean (e.g., height of the boundary layer) that are not included in the simulations.

[41] The reflected radiance at 850 nm measured at an altitude of ∼20 km aboard the ER-2 aircraft with the AVIRIS instrument [*Green et al.*, 1998] at 1243 LT (∼100 min after the ignition) is shown in Figure 13. The signature of the biomass burning plume is easily seen in the enhanced reflectivity, especially over the ocean, where the surface reflectance is negligible. It can be seen that the width of the plume was ∼3 km (using a reflectance of 0.01 W m^{-2} nm^{-1} sr^{-1} as an arbitrary measure of the edge of the plume). Small-scale fluctuations within the plume can be seen.

[42] Figure 14 shows the simulated vertically integrated aerosol mass, which can be compared with the AVIRIS measurements. Using an arbitrary 1 mg m^{-2} isoline to define the edges of the plume, the width of the plume in the model simulation is a little larger than in the observations but still reasonably close. The overall travel distance of the plume is larger in the observations than in the simulations. This was already observed in the comparison with the LIDAR measurements and can be explained by an underestimation of the wind speed over the ocean. Because of the vertically changing horizontal wind speed and direction, as well as the asymmetric fire forcing, the simulations show a horizontal asymmetry. The observed small-scale fluctuations within the plume are not reproduced by the model, because they are caused by small-scale processes (e.g., fluctuations in the fire emissions and small-scale turbulent processes) that are not resolved by the model.

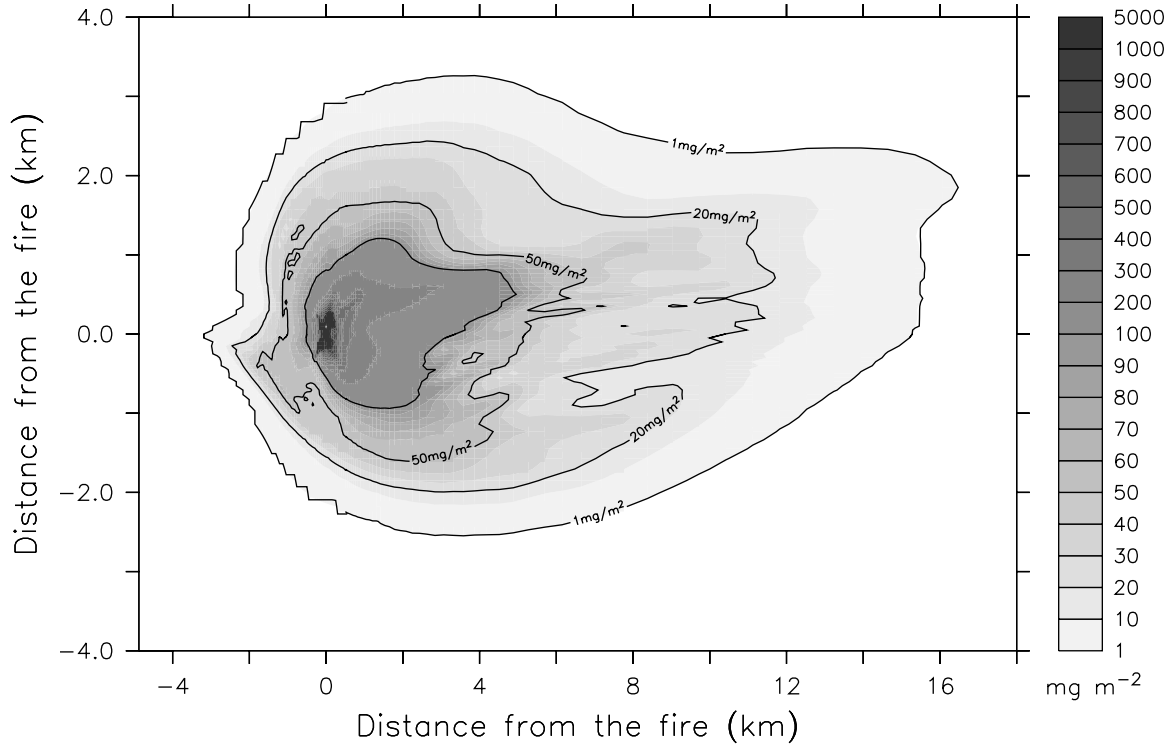

Figure 14. Simulated horizontal extent of the vertically integrated aerosol mass concentrations 100 min after ignition.

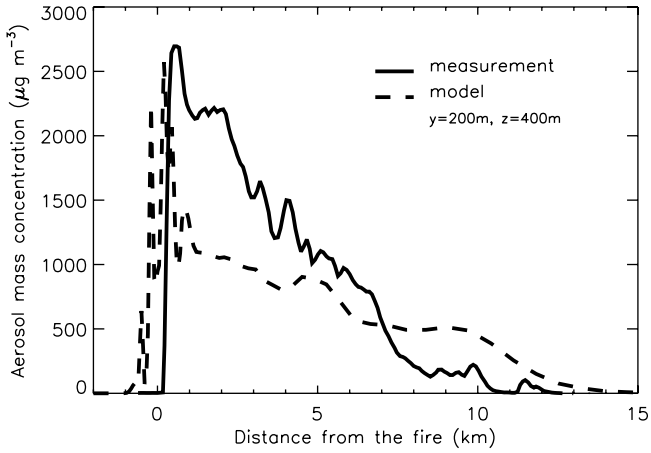

Figure 15. Measured and simulated aerosol mass concentrations along the plume from the Quinault fire. The measurements were performed at 1236 LT (~90 min after ignition) at altitudes between 350 and 500 m. The model results are taken 90 min after ignition along the line at y = 200 m, z = 400 m.

5.1.2. In situ measurements. [43] In this section we use the in situ measurements made aboard the University of Washington's Convair C-131A research aircraft to evaluate the model results. The aircraft flew several times along and across the plume. Aerosol samples were obtained as well as measurements of the optical properties of the smoke. Unfortunately, there were no direct high-resolution measurements of aerosol mass concentrations to compare with the model results. However, aerosol mass concentrations were determined from filter samples taken during three encounters with the plume from the Quinault fire and two other fires during the SCAR-C experiment [*Martins et al.*, 1996]. Using the filter data from all three fires during SCAR-C and simultaneous measurements of the light-scattering coefficient at 538 nm, the dry aerosol mass scattering efficiency was determined to be 3.8 ± 0.2 m^2 g^{-1} [*Hobbs et al.*, 1996; *Reid*, 1998]. By multiplying the high-resolution measurements of the scattering coefficient by the mass-scattering efficiency, the aerosol mass concentrations can be approximated with high temporal and spatial resolution.

[44] Figure 15 shows the measured aerosol mass concentration along the plume and the model results 90 min after ignition. The measurements were performed at 1236 LT (~90 min after ignition). Particle mass concentrations exceeding 2500 μg m^{-3} were observed near the fire; these are consistent with the values of 1820 and 2880 μg m^{-3} given by *Martins et al.* [1996] for the Quinault fire. Downwind of the fire, the mass concentrations decreased gradually with distance from the fire, reaching the background concentration at 13 km downwind. The model also shows the highest particle mass concentrations, which are similar to the observed values but with higher variability, above the fire. However, the mass concentrations from the model are significantly lower (by up to a factor of 2) than the measurements up to 8 km downwind, and the model results are greater than the measurements between 8 and 15 km downwind.

[45] The most plausible reason for the differences between the model results and the measurements is an underestimation of the fire emissions at the beginning phase of the fire by the EPM model. Although the EPM model predicts a strong increase in aerosol emissions after 60 min (see Figure 4), the visible observations showed a strong increase in fire emissions already around 40 min after ignition [*Hobbs et al.*, 1996]. Additionally, the emission factors used in the EPM model might be too low

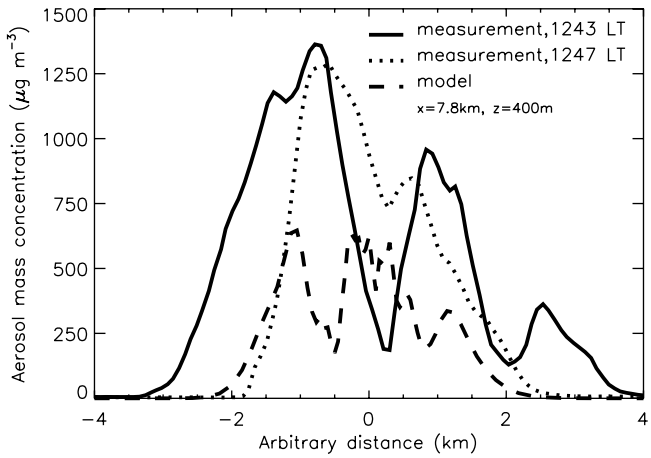

Figure 16. Measured and simulated aerosol mass concentrations across the plume from the Quinault fire. Shown are mass concentrations measured during two transects of the plume (perpendicular to the main axis) at 1243 and 1247 LT (~100 min after ignition) between 8.5- and 10.5-km distance from the fire at altitudes between 430 and 530 m. The model results are taken 100 min after ignition along the line at x = 7.8 km, z = 400 m.

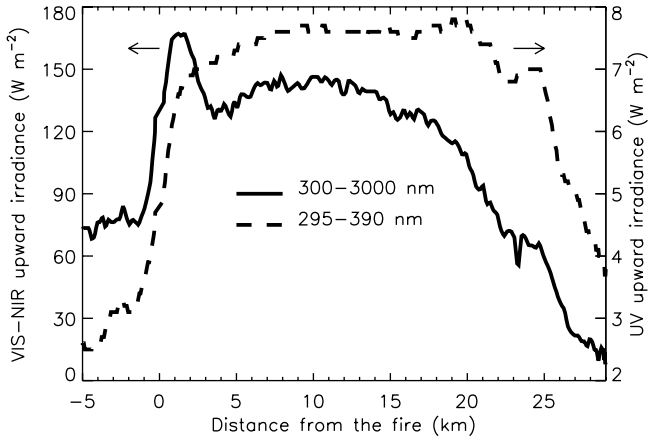

Figure 17. Measured upward radiative fluxes in the wavelength intervals 300–3000 nm (total, solid line, left scale) and 295–390 nm (UV, dashed line, right scale) above the plume. These measurements were obtained between 1254 and 1259 LT at an altitude of ~1350 m simultaneously with the LIDAR measurements shown in Figure 9.

for this scenario. The difference between the observed and simulated aerosol mass concentrations beyond 8 km is probably due to the fact that the aircraft did not fly within the center of the plume at these distances.

[46] Shown in Figure 16 are the measured and simulated aerosol mass concentrations perpendicular to the main plume axis. The measurements were obtained at 1243 and 1247 LT (~100 min after ignition) ~8 km downwind of the fire. The two measured aerosol concentrations differ in their horizontal extent and in their shape even though they were obtained close to each other (in space and time). This reflects the strong inhomogeneities within the plume, which are not reproduced by the model simulations. As mentioned previously, the measured concentrations are nearly twice the simulated concentrations. Nevertheless, the simulated aerosol concentrations show similarities with the measurements. The simulated aerosol concentrations in the plume have three local maxima, which are also present in the measurements at 1243 LT. The width (4 km) of the simulated plume is very close to the measured value during the aircraft crossing at 1247 LT.

[47] It is interesting to compare the measured aerosol mass concentrations across and along the plume. At a distance of 8 km, the concentrations along the plume in Figure 15 are considerably lower than the maximum value shown in Figure 16. This supports our hypothesis that during the end of the plume transect at 1236 LT the aircraft did not fly along the main axis of the plume.

[48] Overall, ATHAM is able to predict the observed aerosol mass concentration and its variability along and across the plume reasonably well. Together with the results from Section 5.1.1, we conclude that ATHAM reproduced the general features within the biomass-burning plume and thus can be used for further sensitivity studies of the processes within the plume.

5.1.3. Radiative fluxes. [49] A comparison of the measured and simulated upward radiation above the smoke plume is presented here.

[50] Aboard the University of Washington's Convair C-131A aircraft were broadband upward and downward looking ultraviolet (UV) (295- to 390-nm) and ultraviolet-visible-near-infrared (UV-VIS-NIR) (300- to 3000-nm) pyranometers.

[51] Shown in Figure 17 are the measured upward fluxes in the UV-VIS-NIR and the UV for a flight transect above the plume of the Quinault fire from 1254 to 1259 LT (~110 min after ignition) at an altitude of ~1350 m. There is a strong increase in the scattered flux over the fire in both wavelength regions, whereas at ~2 km downwind the UV-VIS-NIR flux shows a decrease that is not seen in the UV flux. Both fluxes stay more or less constant over most of the distance along the plume, until they decrease to background values. The background value of UV-VIS-NIR irradiance at the end of the transect (~10 W m^{-2}) is significantly lower than at the start of the transect (~75 W m^{-2}), whereas the change in the background values in the UV is not significant.

[52] To simulate the upward radiative fluxes, only the aerosol from the fire is taken into account and the aerosol mass concentrations simulated after 100 min of fire emissions were used. The solar zenith angle (SZA) was set to 47°, corresponding to the time and place of the observations in Figure 17. The simulations were performed with the PIFM model included in ATHAM and are therefore restricted to the available spectral bands (see Table 1). They are not identical to the measured spectral bands, but for the purpose of this study the first spectral band of the radiative transfer model (200–690 nm) (UV-VIS) can be used for comparison with the UV measurements. The full spectral range of the simulations (UV-VIS-NIR) (200–4000 nm) is used for comparison with the UV-VIS-NIR measurements. The wavelength regions 200–300 nm and 3000–4000 nm do not contribute significantly to the solar energy near the surface.

[53] Figure 18 shows the model results in the UV-VIS (200–690 nm) and UV-VIS-NIR (200–4000 nm) wavelength region of the upward fluxes together with the aerosol optical depth at 550 nm. Over land the simulated values outside of the plume (left sides of Figures 17 and 18) are significantly higher than the measurements (110 W m^{-2} compared to 75 W m^{-2} in the UV-VIS-NIR). A comparison of the UV-VIS-NIR downward flux shows that this was also overestimated by the model (measurement, 712 W m^{-2}; model, 757 W m^{-2}). This underestimation of extinction of incoming solar radiation in the model simulations may be explained by the neglect of aerosol extinction in the absence of smoke. Additional uncertainty in the simulated upward radiation arises from limited information on the surface albedo. Over the ocean the simulated upward flux in the UV-VIS-NIR is also overestimated (35 W m^{-2} compared to 10 W m^{-2}). Further comparisons below focus on the change in the upward fluxes, rather than their absolute values.

[54] As we have seen, the total distance traveled by the smoke in a given time is underestimated by the model, probably because a too low wind speed over the ocean was used in the model. In the simulations as well as in the measurements, the reflected flux in the UV-VIS-NIR over land is much higher than over the ocean (right sides of the Figures 17 and 18), whereas this feature is not significant in the UV and UV-VIS. This behavior is explained by

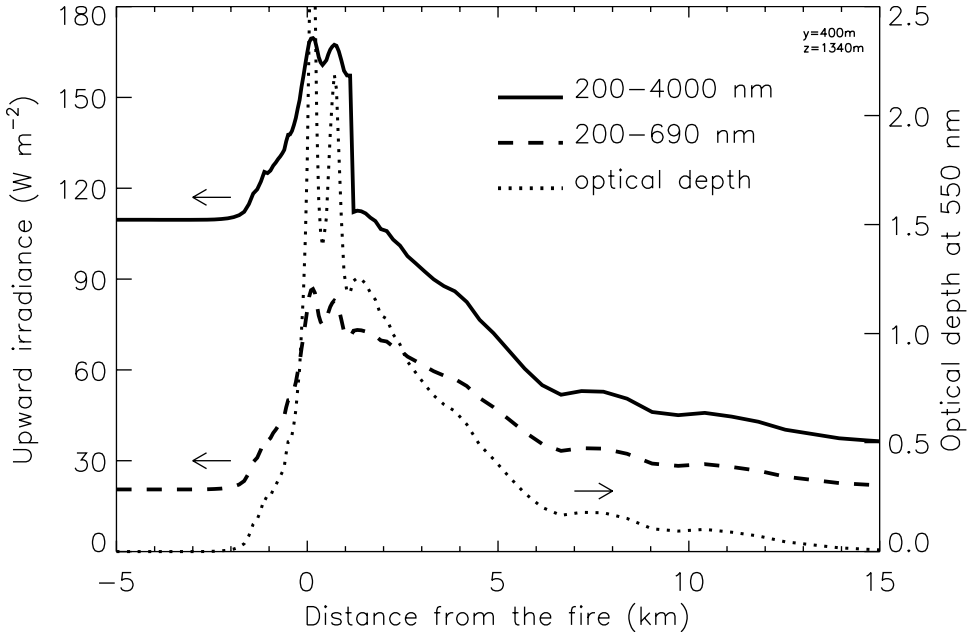

Figure 18. Simulated upward fluxes in the wavelength intervals 200–4000 nm (solid line) and 200–700 nm (dashed line) above the plume at an altitude of 1340 m and a horizontal distance from the center of the fire of 400 m. The solar zenith angle was set to 47°. Also included is the simulated optical depth at 550 nm (dotted line).

the wavelength dependence of the surface albedo over land, which strongly increases for wavelengths longer than 700 nm.

[55] As seen in the measurements, the simulations also show a strong increase in the upward flux above the plume. Also, the sharp decrease in the UV-VIS-NIR flux is observed at ~2 km downwind, but the UV-VIS radiation does not change. In the model simulations this decrease is due to the changing surface albedo for the UV-VIS-NIR in passing from land to ocean (albedo changes from 14.8 to 4.1%). This effect is not significant in the UV-VIS (albedo changes from 4.0 to 4.3%). This suggests that the decrease in the observed UV-VIS-NIR fluxes shown in Figure 17 is due to the change in the surface albedo, although it is more gradual. This hypothesis is supported by the fact that there was no observed decrease in the UV flux.

[56] Downwind of the plume, the measurements show a constant flux in both the UV-VIS and UV-VIS-NIR ranges, but the simulated fluxes decrease. The reason for this different behavior is the decrease in the aerosol optical depth in the model downwind the plume, which is not as pronounced in the observations [*Gassó and Hegg*, 1998]. The low variability in the observed fluxes might be due to the absorbing properties of the aerosol which lead to a saturation of the reflected flux at high optical depth.

[57] Overall, the reflected fluxes above the plume are underestimated by the model, although the background values are too high. This might arise from too low aerosol concentrations or too low backscattering of the aerosols or most probably a combination of both. As we have seen, the simulated aerosol mass concentrations are too low. Artificially increasing the aerosol loading by a factor of 4 in the simulation leads to values for the reflected flux close to the observations (not shown). Additional uncertainties arise from the aerosol properties, for example, size distribution, composition, and state of mixing. The use of the refractive index of soot for the measured BC content of the aerosol may lead to an overestimation of the aerosol absorption. The black carbon determined by thermal or optical techniques from biomass-burning aerosols is not necessarily identical to soot [*Novakov and Corrigan*, 1995; *Mayol-Bracero et al.*, 2002]. However, as long as no further data are available, the use of the refractive index of soot is the only appropiate way to account for BC. Additionally, the assumed internal mixing of the aerosol as well as the use of the same density for OC and BC lead to high aerosol absorption.

[58] For a more realistic comparison, three-dimensional radiative transfer simulations will be performed in future studies.

[59] It is interesting that a systematic underestimation of the aerosol optical depth from biomass-burning aerosol is also found on a global scale, especially in the source regions [*Tegen et al.*, 1997]. Together with the results presented here, this points to uncertainties in the direct aerosol emission from biomass burning. Further studies using a combination of small-scale and regional to global models may help to reduce this discrepancy.

6. Calculation of the Radiative Forcing

[60] In this section the simulated aerosol concentrations are used to calculate the instantaneous direct radiative forcing at the top of the atmosphere (TOA) in the solar spectrum produced by the smoke from the Quinault fire. For this purpose, two radiative transfer simulations are performed: one including and one neglecting the radiative effects of the smoke particles. The solar zenith angle was set to 47° in accord with the observations shown in Figure 17. The aerosol radiative forcing is calculated as the difference in the net flux at TOA between the two simulations (Figure 19).

[61] The radiative forcing is negative for both surface albedos, because the outgoing radiation at TOA increases owing to the presence of the aerosol particles for both cases. The highest forcings are over the ocean even though the optical thickness is lower than over land, because the surface albedo over the ocean (4.1%) is much lower than over the land (14.8%).

[62] The correlation between the optical depth and the aerosol radiative forcing is shown in Figure 20. The instantaneous forcing for an optical depth of unity at 550 nm is −35.8 and −58.0 W m^{-2} for land and ocean, respectively. The radiative forcing in the first spectral band of the radiative transfer model (200–690 nm) is calculated to be −38.2 W m^{-2} for the two

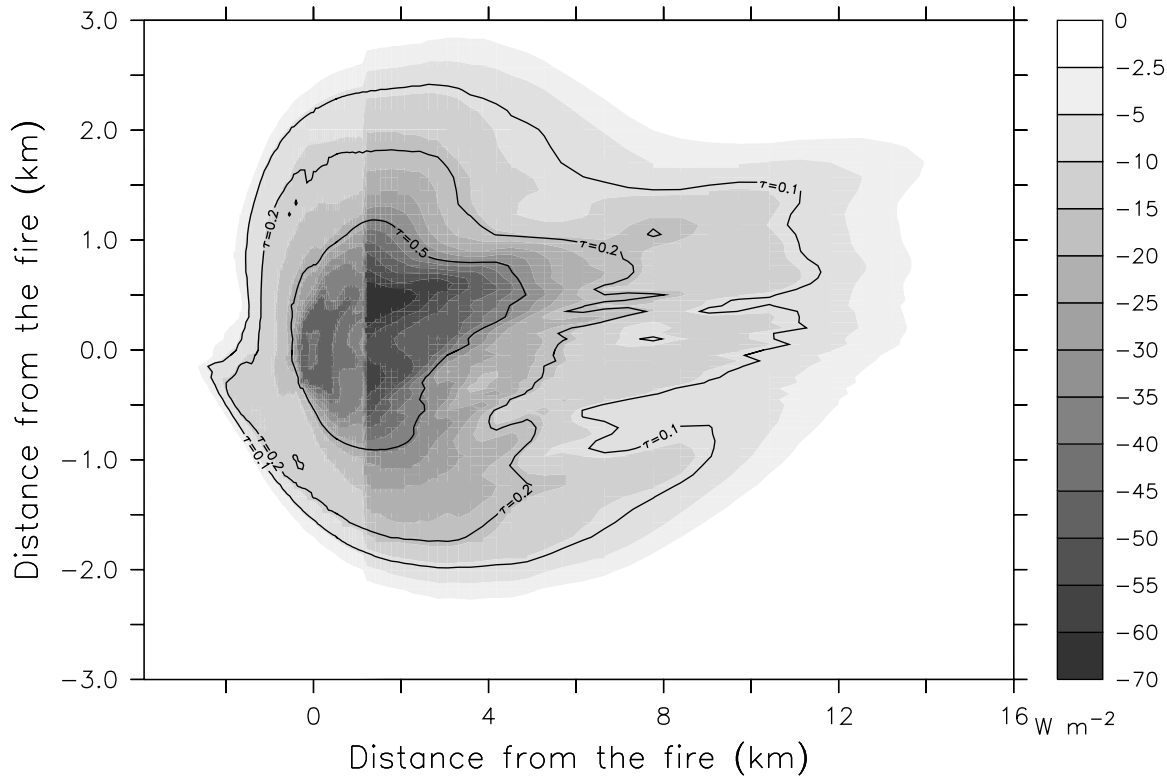

Figure 19. Simulated instantaneous shortwave aerosol radiative forcing for 47° SZA at the top of the atmosphere of the plume from the Quinault fire. The contour lines represent the aerosol optical depth at 550 nm.

surface albedos for an optical depth of unity (not shown). This value can be compared to the measured radiative forcing between 400 and 700 nm of −55 W m^{-2} for an optical depth of unity [*Kaufman*, 1999]. This comparison underlines the fact that the calculated radiative forcing has to be considered as a lower limit estimate. It is interesting that the radiative forcing in the short-wavelength region over land is larger than over the total solar spectrum. This effect is explained by the low single-scattering albedo of the particles at longer wavelengths (see Figure 6), leading to a positive forcing at these wavelengths.

[63] Also included in Figure 20 is the calculated radiative forcing using the following modified form of equation (8) given by *Chylek and Wong* [1995]:

$$\Delta F_R = -F_{\downarrow}(\theta_0, z_0) T_{\text{atm}} \left[(1-A)^2 2\beta(\theta_0)(1-\omega)\tau - 4A\omega\tau\right], \quad (1)$$

where ΔF_R is the direct aerosol radiative forcing, $F_{\downarrow}(\theta_0, z_0)$ is the downward solar flux above the aerosol layer at a solar zenith angle θ_0 and an altitude z_0, T_{atm} is the transmittance of

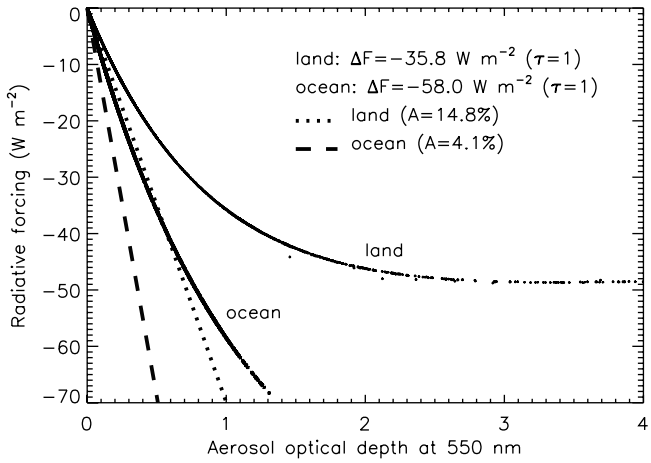

Figure 20. Correlation between the simulated aerosol radiative forcing at the top of the atmosphere and the aerosol optical depth at 550 nm. Also included are calculations of the aerosol radiative forcing using equation (1) for the two surface albedos (dotted and dashed line). The parameters used in the equation are given in the text.

the atmosphere, A is the surface albedo, $\beta(\theta_0)$ is the fraction of radiation scattered by aerosol particles into the upper hemisphere (upscatter fraction as defined by *Wiscombe and Grams* [1976]), ω is the single-scattering albedo, and τ is the optical depth. Equation (1) gives the radiative forcing for an optically thin aerosol layer ($\tau \ll 1$), including the effect of absorbing aerosols.

[64] In the case considered here the downward flux above the aerosol layer was calculated to be 740 W m^{-2}. For the surface albedo the broadband values of 14.8% and 4.1% for land and ocean are used. For ω and $\beta(\theta_0)$ the values at 550 nm (0.848 and 0.175, respectively) are used. The value for $\beta(\theta_0)$ is calculated for θ_0 = 47°. For the transmittance T_{atm} = 0.75, taken from the model simulations for the total solar spectrum.

[65] Equation (1) overestimates the radiative forcing calculated with the radiative transfer model even for small optical depths. The slopes of a linear fit to the results from the radiative transfer simulations for small optical depths are −61.6 and −92 W m^{-2} for land and ocean surface, respectively. The corresponding slopes using (1) are −69.9 and −137.6 W m^{-2}. Both (1) and the radiative transfer calculations show a strong dependence on the surface albedo. This has been reported in other studies [*Ross et al.*, 1998; *Christopher et al.*, 2000a], and it is also visible in global calculations of the direct radiative effect of biomass-burning aerosols [*Penner et al.*, 1998].

[66] Another important feature of Figure 20 is the saturation of the radiative forcing at higher optical depths due to multiple scattering and absorption. The saturation is more prominent over land. This has been shown in earlier radiative transfer simulations [*Ross et al.*, 1998; *Christopher et al.*, 2000a] and observations [*Christopher et al.*, 2000b]. This effect is neglected in (1), and it is obvious that the formula strongly overestimates the radiative forcing of absorbing aerosol at higher optical depths. Therefore, as pointed out by *Chylek and Wong* [1995], use of this formula should be limited to small optical depths.

7. Conclusions

[67] For the first time a model simulation of the atmospheric evolution of a biomass-burning plume and a comparison with measurements were presented. The plume model ATHAM was used to simulate the atmospheric transport of aerosol particles emitted from a prescribed fire on the basis of information on the fire emissions and atmospheric conditions. The simulated aerosol mass concentrations were compared with remote-sensing and in situ measurements of the plume. The injection height and the general behavior of the plume are reproduced with good accuracy by the model. The absolute value of the aerosol mass concentrations shows an underestimation roughly by a factor of 2, probably owing to an underestimation of the fire emissions. Other differences were attributed to the simplified description of the meteorological situation and small-scale features that cannot be resolved in this kind of model. Modeled and measured results for the reflected solar fluxes above the plume were also compared. The impact of the changing surface albedo on the reflected radiation is clearly seen in both the model simulations and the measurements. The model underestimates the upward reflected solar flux, which is mostly attributed to the underestimation of the aerosol concentrations. Additionally, the aerosol absorption might be overestimated owing to assumptions on the state of mixing, the density of OC and BC, and the use of the refractive index of soot for BC. Calculations of the radiative forcing show a strong dependence on surface albedo as well as the saturation effect at higher optical depths. The latter limits the use of linear calculations to very small optical depths.

[68] Overall, we conclude that ATHAM is able to reproduce well the general features of a biomass-burning plume. Combined with a microphysical and a chemical module, ATHAM will be used in future studies to examine the interaction between transport, chemistry, and aerosol and cloud microphysics within biomass-burning plumes. This kind of model has the potential, especially in combination with coordinated field experiments, to substantially increase our understanding of the processes within biomass-burning plumes and improve the representation of vegetation fires within large-scale models.

[69] **Acknowledgments.** This research was supported by the German Ministry for Education and Research (BMBF) under grant 07 AF 308, by NASA grant NAG5-7675 to the University of Washington, and by the German Max Planck Society. We thank Christiane Textor, Michael Herzog, Josef Oberhuber, Carol Strametz, Sue Ferguson, Santiago Gassó, Olivier Boucher, Yoram Kaufman, and Rong-Rong Li for their support. We thank also MIT Press for permission to reproduce Figures 1, 9, and 11.

References

Anderson, G. P., S. A. Clough, F. X. Kneizys, J. H. Chetwynd, and E. P. Shettle, AFGL atmospheric constituent profiles (0–120 km), *AFGL Tech. Rep. AFGL-TR-86-0110*, Air Force Geophys. Lab., Hanscom Air Force Base, Bedford, Mass., 1986.

Andreae, M. O., J. Fishman, and J. Lindesay, The Southern Tropical Atlantic Region Experiment (STARE): Transport and Atmospheric Chemistry near the Equator-Atlantic (TRACE A) and Southern African Fire-Atmosphere Research Initiative (SAFARI): An introduction, *J. Geophys. Res.*, *101*, 23,519–23,520, 1996.

Bohren, C. F., and D. R. Huffman, *Absorption and Scattering of Light by Small Particles*, John Wiley, New York, 1983.

Briegleb, B. P., P. Minnis, V. Ramanathan, and E. Harrison, Comparison of regional clear-sky albedos inferred from satellite observations and model computations, *J. Clim. Appl. Meteorol.*, *25*, 214–226, 1986.

Chatfield, R. B., J. A. Vastano, L. Li, G. W. Sachse, and V. S. Connors, The Great African plume from biomass burning: Generalizations from a three-dimensional study of TRACE A carbon monoxide, *J. Geophys. Res.*, *103*, 28,059–28,077, 1998.

Christopher, S. A., J. Chou, J. Zhang, X. Li, T. A. Berendes, and R. M. Welch, Shortwave direct radiative forcing of biomass burning aerosols estimated using VIRS and CERES data, *Geophys. Res. Lett.*, *27*, 2197–2200, 2000a.

Christopher, S. A., X. Li, R. M. Welch, J. S. Reid, P. V. Hobbs, T. F. Eck, and B. Holben, Estimation of surface and top-of-atmosphere shortwave irradiance in biomass-burning regions during SCAR-B, *J. Appl. Meteorol.*, *39*, 1742–1753, 2000b.

Chylek, P., and J. Wong, Effect of absorbing aerosols on global radiation budget, *Geophys. Res. Lett.*, *22*, 929–931, 1995.

Clark, T. L., M. A. Jenkins, J. Coen, and D. Packham, A coupled atmosphere-fire model: Convective feedback on fire-line dynamics, *J. Appl. Meteorol.*, *35*, 875–901, 1996.

Crowley, W. P., Numerical advection experiments, *Mon. Weather Rev.*, *96*, 1–11, 1968.

Crutzen, P. J., and M. O. Andreae, Biomass burning in the tropics: Impact on atmospheric chemistry and biogeochemical cycles, *Science*, *250*, 1669–1678, 1990.

Crutzen, P. J., and G. R. Carmichael, Modeling the influence of fires on atmospheric chemistry, in *Fire in the Environment: The Ecological, Atmospheric, and Climatic Importance of Vegetation Fires*, pp. 89–103, edited by P. J. Crutzen and J. G. Goldammer, John Wiley, New York, 1993.

Fenn, R W., S. A. Clough, W. O. Gallery, R. E. Good, F. X. Kneizys, J. D. Mill, L. S. Rothmann, E. P. Shettle, and F. E. Volz, Optical and infrared properties of the atmosphere, in *Handbook of Geophysics and the Space Environment*, edited by A. S. Jursa, pp. 18-1–18-27, Air Force Geophys. Lab., Hanscom Air Force Base, Bedford, Mass., 1985.

Ferguson, S. A., D. V. Sandberg, and R. Ottmar, Modelling the effects of landuse changes on global biomass emissions, in *Biomass Burning and Its Inter-relationships With the Climate System*, edited by J. L. Innes, M. Beniston, and M. M. Verstraete, pp. 33–50, Kluwer Acad., Norwell, Mass., 2000.

Galanter, M., H. Levy II, and G. R. Carmichael, Impacts of biomass burning on tropospheric CO, NO_x, and O_3, *J. Geophys. Res.*, *105*, 6633–6653, 2000.

Gassó, S., and D. A. Hegg, Comparison of columnar aerosol optical properties measured by the MODIS airborne simulator with *in situ* measurements: A case study, *Remote Sens. Environ.*, *66*, 138–152, 1998.

Graf, H.-F., M. Herzog, J. M. Oberhuber, and C. Textor, The effect of environmental conditions on volcanic plume rise, *J. Geophys. Res.*, *104*, 24,309–24,320, 1999.

Grant, K. E., C. C. Chuang, A. S. Grossman, and J. E. Penner, Modeling the spectral optical properties of ammonium sulfate and biomass burning aerosols: Parameterization of relative humidity effects and model results, *Atmos. Environ.*, *33*, 2603–2620, 1999.

Green, R. O., et al., Imaging spectroscopy and the airborne visible/infrared imaging spectrometer (AVIRIS), *Remote Sens. Environ.*, *65*, 227–248, 1998.

Grishin, A. M., Mathematical modelling of forest fires, in *Fire in Ecosystems of Boreal Eurasia*, edited by J. G. Goldammer and V. V. Furyaev, pp. 285–302, Kluwer Acad., Norwell, Mass., 1996.

Herring, J. A., and P. V. Hobbs, Radiatively driven dynamics of the plume from 1991 Kuwait oil fires, *J. Geophys. Res.*, *99*, 18,809–18,826, 1994.

Herzog, M., H.-F. Graf, C. Textor, and J. M. Oberhuber, The effect of phase changes of water on the development of volcanic plumes, *J. Volcanol. Geotherm. Res.*, *87*, 55–74, 1998.

Hobbs, P. V., L. F. Radke, J. H. Lyons, R. J. Ferek, D. J. Coffman, and Thomas J. Casadevall, Airborne measurements of particles and gas emissions from the 1990 volcanic eruptions of Mount Redoubt, *J. Geophys. Res.*, *96*, 18,735–18,752, 1991.

Hobbs, P. V., J. S. Reid, J. A. Herring, J. D. Nance, R. E. Weiss, J. L. Ross, D. A. Hegg, R. D. Ottmar, and C. Liousse, Particle and trace-gas measurements in the smoke from prescribed burns of forest products in the Pacific Northwest, in *Biomass Burning and Global Change*, edited by J. S. Levine, pp. 697–715, MIT Press, Cambridge, Mass., 1996.

Holben, B. N., Y. J. Kaufman, A. W. Setzer, D. D. Tanre, and D. E. Ward, Optical properties of aerosol emissions from biomass burning in the tropics, BASE-A in *Global Biomass Burning: Atmospheric, Climatic, and Biospheric Implications*, edited by J. S. Levine, pp. 403–411, MIT Press, Cambridge, Mass., 1991.

Horvath, H., Atmospheric light absorption-A review, *Atmos. Environ.*, *27A*, 293–317, 1993.

Kaufman, Y., Direct radiative forcing of smoke at the top and bottom of the atmosphere, poster presented at Sixth Scientific IGAC Conference, Int. Global Atmos. Chem. Proj., Bologna, Italy, 1999.

Kaufman, Y. J., L. A. Remer, R. D. Ottmar, D. E. Ward, R.-R. Li, R. Kleidman, R. S. Fraser, L. Flynn, D. McDougal, and G. Shelton, Relationship between remotely sensed fire intensity and rate of emission of smoke: SCAR-C experiment, in *Biomass Burning and Global Change*, edited by J. S. Levine, pp. 685–696, MIT Press, Cambridge, Mass., 1996.

Kaufman, Y. J., et al., Smoke, Clouds, and Radiation-Brazil (SCAR-B) experiment, *J. Geophys. Res.*, *103*, 31,783–31,808, 1998.

Kotchenruther, R. A., and P. V. Hobbs, Humidification factors of aerosols from biomass burning in Brazil, *J. Geophys. Res.*, *103*, 32,081–32,089, 1998.

Krekov, G. M., Models of atmospheric aerosols, in *Aerosol Effects on Climate*, edited by S. G. Jennings, pp. 9–72, Univ. of Ariz. Press, Tucson, 1992.

Langmann, B., M. Herzog, and H.-F. Graf, Radiative forcing of climate by sulfate aerosols as determined by a regional circulation chemistry transport model, *Atmos. Environ.*, *32*, 2757–2768, 1998.

Liousse, C., J. E. Penner, C. Chuang, J. J. Walton, H. Eddleman, and H. Cachier, A global three-dimensional model study of carbonaceous aerosols, *J. Geophys. Res.*, *101*, 19,411–19,432, 1996.

Loughlin, P. E., T. Trautmann, A. Bott, W. G. Panhans, and W. Zdunkowski, The effect of different radiation parameterizations on cloud evolution, *Q. J. R. Meteorol. Soc.*, *123*, 1985–2007, 1997.

Martins, J. V., P. Artaxo, P. V. Hobbs, C. Liousse, H. Cachier, Y. Kaufman, and A. Plana-Fattori, Particle size distribution, elemental composition, carbon measurements, and optical properties of smoke from biomass burning in the Pacific Northwest of the United States, in *Biomass Burning and Global Change*, edited by J. S. Levine, pp. 716–732, MIT Press, Cambridge, Mass., 1996.

Mayol-Bracero, O. L., P. Guyon, B. Graham, G. Roberts, M. O. Andreae, S. Decesari, M. C. Facchini, S. Fuzzi, and P. Artaxo, Water-soluble organic compounds in biomass-burning aerosols over Amazonia, 2, Apportionment of the chemical composition and importance of the polyacidic fraction, *J. Geophys. Res.*, in press, 2002.

McCarter, R. J., and A. Broido, Radiative and convective energy from wood crib fires, *Pyrodynamics*, *2*, 65–85, 1965.

McDow, S. R., M. Jang, Y. Hong, and R. M. Kamens, An approach to studying the effect of organic composition on atmospheric aerosol photochemistry, *J. Geophys. Res.*, *101*, 19,539–19,600, 1996.

Novakov, T., and C. E. Corrigan, Thermal characterization of biomass smoke particles, *Mikrochim. Acta*, *119*, 157–166, 1995.

Oberhuber, J. M., M. Herzog, H.-F. Graf, and K. Schwanke, Volcanic plume simulation on large scales, *J. Volcanol. Geotherm. Res.*, *87*, 29–53, 1998.

Penner, J. E., L. C. Haselman Jr., and L. L. Edwards, Smoke-plume distribution above large-scale fires: Implications for simulations of "Nuclear Winter", *J. Clim. Appl. Meteorol.*, *25*, 1434–1444, 1986.

Penner, J. E., M. M. Bradley, C. C. Chuang, L. L. Edwards, and L. F. Radke, A numerical simulation of the aerosol-cloud interaction and atmospheric dynamics of the Hardiman township, Ontario, prescribed burn, in *Global Biomass Burning: Atmospheric, Climatic, and Biospheric Implications*, edited by J. S. Levine, pp. 420–426, MIT Press, Cambridge, Mass., 1991.

Penner, J. E., C. C. Chuang, and K. Grant, Climate forcing by carbonaceous and sulfate aerosols, *Clim. Dyn.*, *14*, 839–851, 1998.

Poppe, D., R. Koppmann, and J. Rudolph, Ozone formation in biomass burning plumes: Influence of atmospheric dilution, *Geophys. Res. Lett.*, *25*, 3823–3826, 1998.

Radke, L. F., J. H. Lyons, P. V. Hobbs, and R. E. Weiss, Smokes from the burning of aviation fuel and their self-lofting by solar heating, *J. Geophys. Res.*, *95*, 14,071–14,076, 1990.

Radke, L. F., D. A. Hegg, P. V. Hobbs, J. D. Nance, J. H. Lyons, K. K. Laursen, R. E. Weiss, P. J. Riggan, and D. E. Ward, Particulate and trace gas emissions from large biomass fires in North America, in *Global Biomass Burning: Atmospheric, Climatic, and Biospheric Implications*, edited by J. S. Levine, pp. 209–224, MIT Press, Cambridge, Mass., 1991.

Reid, J. S., Emission, evolution, and radiative properties of particles from biomass burning in Brazil, Ph.D. thesis, Univ. of Wash., Seattle, 1998.

Ross, J. L., P. V. Hobbs, and B. Holben, Radiative characteristics of regional hazes dominated by smoke from biomass burning in Brazil: Closure tests and direct radiative forcing, *J. Geophys. Res.*, *103*, 31,925–31,941, 1998.

Sandberg, D. V., and J. Peterson, A source strength model for prescribed fire in coniferous logging slash, paper presented at 21st Annual Meeting of the Air Pollution Control Association, Portland, Oreg., 1984.

Sloane, C. S., Optical properties of aerosols-Comparison of measurements with model calculations, *Atmos. Environ.*, *17*, 409–416, 1983.

Smolarkiewicz, P. K., A fully multidimensinal positive definite advection transport algorithm with small implicit diffusion, *J. Comput. Phys.*, *54*, 325–362, 1984.

Sutherland, R. A., and R. K. Khanna, Optical properties of organic-based aerosols produced by burning vegetation, *Aerosol Sci. Technol.*, *14*, 331–342, 1991.

Tanré, D., Y. J. Kaufman, M. Herman, and S. Mattoo, Remote sensing of aerosol properties over oceans using the MODIS/EOS spectral radiances, *J. Geophys. Res.*, *102*, 16,971–16,988, 1997.

Tegen, I., P. Hollrig, M. Chin, I. Fung, D. Jacob, and J. Penner, Contribution of different aerosol species to the global aerosol extinction optical thickness: Estimates from model results, *J. Geophys. Res.*, *102*, 23,895–23,915, 1997.

Textor, C., Numerical simulation of scavenging processes in explosive volcanic eruption clouds, Ph.D. thesis, Univ. Hamburg, Hamburg, Germany, 1999.

Toon, O. B., J. B. Pollack, and B. N. Khare, The optical constants of several atmospheric aerosol species: Ammonium sulfate, aluminium oxide, and sodium chloride, *J. Geophys. Res.*, *81*, 5733–5748, 1976.

Wehrli, C., Extraterrestrial solar spectrum, *Publ. 615*, World Radiat. Cent., Davos Dorf, Switzerland, 1985.

Wiscombe, W. J., and G. W. Grams, The backscatter fraction in two stream approximations, *J. Atmos. Sci.*, *33*, 2440–2451, 1976.

Zdunkowski, W. G., W.-G. Panhans, R. M. Welch, and G. J. Korb, A radiation scheme for circulation and climate models, *Contrib. Atmos. Phys.*, *55*, 215–238, 1982.

M. O. Andreae and J. Trentmann, Department of Biogeochemistry, Max Planck Institute for Chemistry, P.O. Box 3060, D-55020 Mainz, Germany. (jtrent@mpch-mainz.mpg.de)

H.-F. Graf, Max Planck Institute for Meteorology, Bundesstrasse 55, D-20146 Hamburg, Germany.

P. V. Hobbs, Department of Atmospheric Sciences, University of Washington, Box 351640, Seattle, WA 98195-1640.

R. D. Ottmar, Seattle Forestry Science Laboratory, 4043 Roosevelt Way N.E., Seattle, WA 98105.

T. Trautmann, Institute for Meteorology, University of Leipzig, Stephanstrasse 3, D-4103 Leipzig, Germany.